ACS OMEGA

Open Access

http://pubs.acs.org/journal/acsodf

Article

Moist Heat Synthesis of Magnetic EGCG-Cappedα-Fe_2O_3 Nanoparticles and Their *In Vitro* and *In Silico* Interactions with Pristine HSA- and NDM-1-Producing Bacteria

Khursheed Ali, Shruti Rakesh, Shamsi Khalid, and Asad U. Khan*

Cite This: *ACS Omega* 2023, 8, 48775−48786

Read Online

ACCESS | Metrics & More | Article Recommendations

ABSTRACT: A simple, facile, moist-heating (*e.g.*, autoclave), one-step procedure for EGCG-mediated biosynthesis of narrow-size magnetic iron oxide (α-Fe_2O_3) nanoparticles (EGCG-MINPs) was developed. The influence of pH of the reaction mixture over the size distribution of as-synthesized EGCG-MINPs was investigated systematically by employing UV−visible (UV−vis) spectroscopy and dynamic light scattering (DLS)-based hydrodynamic size, surface charge (zeta-potential), and polydispersity index (PDI). The FE-SEM, TEM, and XRD characterizations revealed that the EGCG-MINPs synthesized at pH 5.0 were in the size range of 6.20−16.7 nm and possess well-crystalline hexagonal shaped nanostructures of hematite (α-Fe_2O_3) crystal phase. The role of EGCG in Fe^{3+} ion reduction and EGCG-MINP formation was confirmed by FTIR analysis. The VSM analysis has revealed that EGCG-MINPs were highly magnetic nanostructures with the hysteretic feature of saturation magnetization (Ms), remanent magnetization (Mr), and coercivity (Hc) as 33.64 emu/g, 12.18 emu/g, and 0.33 Oe, respectively. Besides, significant ($p < 0.001$) dose-dependent (250−1000 μg/mL) antibacterial and antibiofilm activities against the NDM-1-producing Gram-negative *Escherichia coli* (AK-33), *Klebsiella pneumoniae* (AK-65), *Pseudomonas aeruginosa* (AK-66), and *Shigella boydii* (AK-67) bacterial isolates warranted the as-synthesized EGCG-MINPs as a promising alternative for clinical management of chronic bacterial infections in biomedical settings. In addition, molecular docking experiments revealed that compared to free Fe^{3+} and EGCG alone, the EGCG-MINPs or Fe-EGCG complex possess significantly high binding affinity toward HSA and hence can be considered as promising biocompatible nanodrug carriers in *in vivo* drug delivery systems.

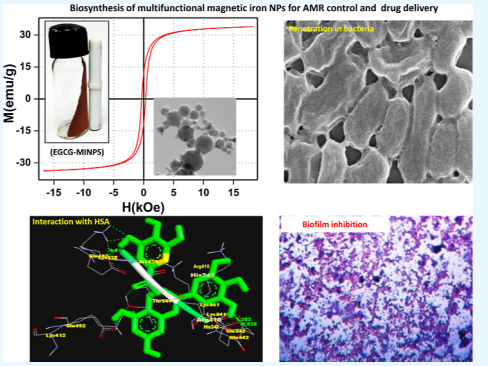

INTRODUCTION

Recently, antimicrobial resistance (AMR) has become one of the most threatening health concerns, globally. According to the latest repot of World Health Organization, 2022 (www.who.int/publications/i/item/no-time-to-wait-securing-the-future-from-drug-resistant-infections),[1] AMR infection can account for around 700,000 deaths per annum, globally, and expected to cumulate to 10 million by 2050, due to the deficit of appropriate control measures. During the last two decades, the AMR landscape has witnessed a drastic emergence of extended-spectrum β-lactamase (ESβL)-producing bacteria. Among lactamases, metallo-β-lactamase (MBL) and Delhi metallo-β-lactamase (NDM) bacteria such as *Klebsiella pneumoniae*, *Enterobacteriaceae*, *Acinetobacter*, and *Pseudomonas* species are known to be notorious in escaping the antibacterial effects of most β-lactam antibiotics including carbapenems.[2] In general, the employment of multiple antibiotics against bacterial infections, with no prior resistance assessment, led the bacteria to be resistant to multiple drugs. Thus, development of multiple drug-resistant (MDR) bacteria jeopardizes the clinical management of AMR significantly.[3]

Besides, the three-dimensional (3D) biofilms of such MDR bacteria, compared to their planktonic cells, are manifold stubborn to be treated with conventional antimicrobials, due to their extremely poor excess to biofilm-enmeshed bacterial cells.[4,5] Majorly, the antibiofilm potential of antimicrobials is focused to mitigate the biofilm establishment by surface treatment strategies. However, such inhibitory strategies are unable to eliminate the biofilm due to poor penetration, distribution, and functional stability of antimicrobials in the harsh microenvironment of established biofilms.[6] The precise treatment relies on the delivery of antimicrobials to targeted biofilms, and thus, it can be argued that deeper penetration and prolonged structural stability of metal and metal-oxide NPs into biofilms increased the delivery of antimicrobials and thus

Received: August 5, 2023
Revised: October 10, 2023
Accepted: October 17, 2023
Published: December 13, 2023

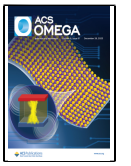

enhanced the antibiofilm efficacy of nanoformulations. Besides, surface functionalization of metal NPs with antimicrobial biogenic entities, such as peptides, polyphenols, enzymes, and so forth, plays a pivotal role in maintaining the NP dispersity, which may facilitate deep penetration, ultimately resulting in biofilm disruption.[4] Nevertheless, appropriate chemical, physical, and optical features with a high surface-to-volume ratio prompt the employment of magnetic NPs as nanocarriers in different anticancer drug delivery systems.[7,8]

Nevertheless, the latest pursuits for the clinical management of antimicrobial resistance (AMR) and associated nosocomial infections have involved numerous metallic nanoparticles (NPs) as nanodrug particles due to their nanoscale-relying unique physicochemical properties. In fact, metallic NPs, typically less than 100 nm in diameter, were endowed with an intrinsic ability to interact and internalized with a wide range of microbial and human cells.[9−11] Nonetheless, despite a plethora of reports on metallic and nonmetallic nanomaterials against the AMR microbes, the quest for novel nanoscale formulations, with desired features, still continues. In fact, every individual feature of NPs, such as size, shape, stability, internalization propensity, drug payload, and delivery can directly alter the antibacterial efficacy of NPs proportionally.[9,12,13] Therefore, scientific interest in the synthesis of desired nanostructures has grown exponentially. Over recent years, researchers have explored several methods, physical, chemical, and biological, to synthesize single-metallic (*e.g.*, Ag, CuO, ZnO, and TiO_2) as well as bimetallic (*e.g.*, $PbWO_4$, $BaFe_{12}O_{19}$, and Ni-$CeZrO_2$) NPs with different sizes, morphologies, and catalytic and antimicrobial activities.[14−19] In biomedical settings, nontoxicity, biocompatibility, fluorescence, dispersity, drug payload, and stability of NPs have been regarded as decisive features in nanodrug delivery system. Thus, due to being a nonhazardous, inexpensive, and safe strategy, the involvement of plant bioactive compounds (*e.g.*, flavanols, tannins, terpenoids, polyphenol, enzymes, *etc.*) in the synthesis of metallic nanoformulations has received enormous attention. To date, several medicinally important phyto-polyphenols including curcumin, quercetin, and chitosan have been employed as metal-reducing, stabilizing, and surface functionalization agents.[11,13,20]

Among several fascinating properties, magnetism in iron oxide NPs is the one which makes them a unique candidate within metallic NPs in different biomedical, clinical, and environmental settings.[4,21,22] The ionic state of iron is trivalent (Fe^{3+}) in four oxides, α-Fe_2O_3 (hematite), γ-Fe_2O_3 (maghemite), β-Fe_2O_3, and ε-Fe_2O_3; Fe_3O_4 (magnetite) and FeO (wüstite) polymorphs possess tetravalent (Fe^{4+}) and bivalent (Fe^{2+}) ions, respectively.[23] Of the four oxides, α-Fe_2O_3 has been used in gas sensors, catalysts, and medicine due to its stability, antiferromagnetic, and n-type semiconducting properties.[24] Importantly, the use of bare surface NPs is toxic, which can minimize their applications in biomedical settings due to undesired interaction between the released Fe ions and biological systems.[25] Through biogenic approaches, the synthesis of magnetic iron oxide NPs ($MINP_S$) is more challenging due to the intrinsic ability of reduced iron to be oxidized in biological milieu more readily as compared to gold and silver. Earlier studies were on on crude green tea (*Camellia sinensis*) leaf extracts, containing several bioactive compounds (proteins, enzymes, carbohydrates, polyphenols, hydrocarbons, catechins, *etc.*), which mediated the synthesis of nonmagnetic α-Fe_2O_3-NPs using high temperature (180 °C), pressure, and prolonged time (13 h) hydrothermal process.[26,27] However, the current study involved a low concentration (1 mM) of one purely bioactive tea catechin, i.e, epigallocatechin-3-gallate (EGCG), among the four abundant catechins: (i) epicatechin (EC), (ii) epicatechin-3-gallate (ECG), (ii) epigallocatechin (EGC), and (iv) epigallocatechin-3-gallate (EGCG) in green tea extract and Fe precursors; low temperature (121 °C) for 20 min was used to overcome the thermal decomposition of surface-adsorbed bioactive EGCG to ensure the size stability and dispersity of EGCG-capped magnetic iron oxide NPs (EGCG-MINPs). Besides, none of the studies have shown the employment of pure EGCG in one-step synthesis methods of highly magnetic EGCG-MINPs and demonstrated the comparative antibacterial and antibiofilm activities against NDM-1-producing Gram-negative bacteria.

Hence, herein, we prepared EGCG-encapsulated magnetic iron oxide NPs (EGCG-MINPs) of <10 nm to investigate their antibacterial and antibiofilm activities against the NDM-1-producing *Escherichia coli* (AK-33), *K. pneumoniae* (AK-65), *Pseudomonas aeruginosa* (AK-66), and *Shigella boydii* (AK-67) clinical bacterial isolates. At the same time, the study has witnessed the effect of reaction pH (3.0−11.0) on EGCG encapsulation around nascent NPs which appeared in the secondary or hydrodynamic size, polydispersity index (PDI), and zeta potential of dispersed EGCG-MINPs. The magnetic hysteresis of the as-prepared EGCG-MINPs on a vibrating sample magnetometer (VSM) has shown 33.64, 12.18, and 0.33 Oe, saturation magnetization (Ms), remanent magnetization (Mr), and coercivity (Hc), respectively. Considering the tremendous biological *in vivo* applications of MINPs like biosensing, diagnostics, and bioimaging, we have also investigated their biocompatibility by exploring the *in silico* interaction of free EGCG, Fe^{3+}, and EGCG-MINPs or Fe-EGCG complex with human serum albumin (HSA). Our molecular docking experiments revealed that compared to free Fe^{3+} and EGCG alone, the EGCG-MINPs or Fe-EGCG complex possess a significantly high binding affinity toward HSA and hence can be considered as promising biocompatible nanodrug carriers in *in vivo* drug delivery systems.

MATERIALS AND METHODS

Chemicals. Epigallocatechin gallate (EGCG) (≥95%, Sigma-Aldrich, CAS no. 989-51-5), iron(III) chloride hexahydrate ($FeCl_3{\cdot}6H_2O$), sodium hydroxide (NaOH, 98%, Thermo Fisher Scientific CAS no. 1310-732), and hydrochloric acid (HCl) (37%, Thermo Fisher Scientific CAS no. 7647-010) were used in magnetic hematite (α-Fe_2O_3-NPs) synthesis. However, for bacterial assays, Luria−Bertani broth (LB), brain−heart infusion broth (BHI), and crystal violet (CV) stain were procured from Hi-media Laboratories, Mumbai, India.

Synthesis of EGCG-Capped Magnetic Iron Nanoparticles. A single-step, EGCG-mediated green synthesis of magnetic α-Fe_2O_3-NPs (EGCG-MINPs) was performed by following the procedure described by Khan *et al.*[9] Precisely, 1 mM $FeCl_3{\cdot}6H_2O$ was prepared in 500 mL of ultrapure MilliQ water at 60 °C with vigorous stirring (800 rpm/min). The as-prepared aqueous $FeCl_3{\cdot}6H_2O$ was divided into five flasks. Each flask containing 100 mL of $FeCl_3{\cdot}6H_2O$ was then treated with NaOH (1N) and HCL (1N) to maintain the pH as 3.0, 5.0, 7.0, 9.0, and 11.0, respectively. EGCG (45.8 mg/100 mL of $FeCl_3{\cdot}6H_2O$) was so added in separate flasks which could maintain the EGCG and Fe concentrations as 1 mM in the

https://doi.org/10.1021/acsomega.3c05743
ACS Omega 2023, 8, 48775−48786

reaction mixtures at varied pH scales (*i.e.*, pH 3.0−11.0).[9] The flasks were transferred to an autoclave and heated at 121 °C and 15 psi pressure for 20 min, three times successively. Next, the reaction mixtures were spun (5000 rpm/min), and red pellets of α-Fe_2O_3-NPs were collected. The pellets were dried in a vacuum oven at 60 °C for 12 h. The magmatic particles were then separated using a magnetic bar. The final dried powder was stored in an air-proof glass vial to use for physicochemical and magnetic characterization and antibacterial studies.

Characterization. *UV−Vis, Dispersion, and Zeta-Potential Analyses of EGCG-MINPs.* The EGCG-MINPs synthesized at pH of 3.0, 5.0, 7.0, 9.0, and 11.0 were dissolved in deionized Milli-Q water (100 μg/mL) and sonicated for 10 min at 30% amplitude (Q-Sonica Sonicator, Q700, USA). 1000 μL of the sonicated aqueous suspensions of α-Fe_2O_3NPs was then added into quarts and disposable plastic cuvettes (DTS1060C and DTS1070C) and analyzed on a double-beam UV−vis spectrophotometer (UV-1800, Shimadzu, USA) and Nano-Sizer ZS (90, Malvern Instrument Ltd., UK), for surface plasmon resonance (SPR), hydrodynamic size by dynamic light scattering (DLS), PDI, and zeta potential measurements, respectively.[9]

Crystallinity, Size, and Morphology of EGCG-MINPs. Considering UV−vis spectra, DLS, PDI, and zeta potential of the EGCG-MINPs prepared at pH 5.0 were further investigated for crystallinity, average particle size, and crystal phase, on a MiniFlex II benchtop XRD system (Rigaku Corporation, Tokyo, Japan) operating at 40 kV and a current of 30 mA with Cu K_α radiation (k = 1.54 Å). The average crystalline size of the Fe_2O_3NPs was calculated following Debye−Scherrer's formula, described elsewhere.[15] Besides, for morphological characteristics, *i.e.,* shape and size, the dried powder of EGCG-MINPs was analyzed by employing a transmission electron microscope (JEOL, Japan) and a field-emission scanning electron microscope (JEOL, Japan). However, ImageJ image-analyzing software was used to assess the average and distribution of size of the particles in FE-SEM and TEM images.[28]

Surface and Magnetism Analyses of EGCG-MINPs. To investigate the possible components of EGCG adsorbed on the surface of EGCG-MINPs, FTIR spectral analysis was carried out. Precisely, dried EGCG-MINPs were mixed with spectroscopic KBr in 1:100 ratio. The spectrum was recorded in diffuse reflectance mode at a resolution of 4 cm^{-1} in KBr pellets. For magnetic measurements, EGCG-MINPs were analyzed by employing a quantum design vibrating sample magnetometer (VSM; EV7, ADE).[29]

Antibacterial Potential of EGCG-MINPs against NDM-1 Bacterial Isolates. MIC and MBC Determination of EGCG-MINPs. The minimum inhibitory concentrations (MICs) and minimum bactericidal concentrations (MBCs) were determined by growing the bacterial cultures with 250−2000 μg/mL of EGCG-MINPs, as described by Ali *et al.*[15] Twofold dilution method was followed to determine the MICs and MBCs of EGCG-MINPs against New Delhi metallo-beta-lactamase-1 (NDM-1)-producing *E. coli* (AK-33), *K. pneumoniae* (AK-65), *P. aeruginosa* (AK-66), and *S. boydii* (AK-67), in LB medium. In brief, freshly grown bacterial cells (log phase) were incubated with 250−2000 μg/mL of EGCG-MINPs in triplicate. Untreated bacterial cells and medium containing NPs were used as positive and negative controls, respectively. The cells were allowed to grow in the presence of 250−2000 μg/mL of EGCG-MINPs at 37 °C, 120 rpm for 12 h. After incubation, the optical densities (ODs) were measured at 600 nm by using a 96-well microtiter plate reader (BIORAD iMark TM Microplate Reader, India). The $OD_{600\ nm}$ values were normalized by subtracting the absorbance of negative controls. More than 80% reduction in $OD_{600\ nm}$ in bacterial survival was considered as MICs of EGCG-MINPs against the bacterial strains.

EGCG-MINP-Induced Morphological Damage in Bacterial Cells. EGCG-MINP-induced morphological damage in bacterial cells was examined by analyzing untreated and treated cells by SEM. In brief, untreated and EGCG-MINP-treated (at MIC/2, 37 °C for 24 h) bacteria cells were spun at 3000 rpm, for 5 min. The pellets of bacterial cells were fixed in glutaraldehyde (2.5%, 4 °C, 4 h) and then dehydrated with a series of alcohols (30, 50, 70, and 90%). Next, 50 μL of the bacterial cell suspension was spread on a clean glass coverslip. The as-prepared thin films of bacteria were coated with gold and finally mounted on a SEM stub to visualize the interaction between bacteria and EGCG-MINPs as well as the resultant morphological damage in the treated bacterial cells.[30]

EGCG-MINP Dose-Dependent Biofilm Inhibition. Biofilm formation assay was carried out in 96-well microtiter plates.[9] Briefly, 20 μL of freshly grown bacterial cells ($OD_{600\ nm}$ = 0.5), *E. coli* (AK-33), *K. pneumoniae* (AK-65), *P. aeruginosa* (AK-66), and *S. boydii* (AK-67), were seeded into designated wells. Next, 200 μL of LB medium containing EGCG-MINPs (250−1000 μg/mL) was added into the respective wells. Besides, EGCG-MINPs (250−1000 μg/mL) and bacterial cell suspensions in LB medium were taken as negative and positive controls, respectively. The microwell plates were then incubated at 37 °C for 24 h. After 24 h, the suspensions in the wells were aspirated gently by using a micropipette without disturbing the established biofilms. The wells were dried for 20 min at room temperature. Wells were added 200 μL of 0.25% crystal violet stain and kept at 37 °C for 30 min. Next, the wells were washed and air-dried, and then the bound stain was solubilized in 200 μL of 95% ethanol. The absorbance was recorded at 620 nm by use of a microplate reader (iMark Microplate Reader, Bio-Rad, 1681130, USA).[31]

Microscopic Analysis of EGCG-MINP-Induced Biofilm Inhibition. For microscopic biofilm analysis, sterilized coverslips (1 × 1 cm) were first placed into the wells of a 12-well polystyrene tissue culture plate. LB media (5 mL) containing EGCG-MINPs (250−1000 μg/mL) was added to the designated wells. 200 μL of freshly grown *E. coli*, *K. pneumoniae*, *Escherichia Aeruginosa,* and *S. boydii* cells (~10^7 cfu/mL) were added to the respective wells. Untreated control cells (positive control) in LB medium were run parallel. The plate was incubated at 37 °C for 24 h. After 24 h, cover glasses with the established biofilms were removed from the wells with forceps, dipped in PBS to remove unbound bacterial cells, and placed on cleaned glass slides. The biofilms were allowed to dry for 30 min in air. The biofilms were then stained with crystal violet (0.25%) for 10 min and then washed with PBS. Finally, the biofilms were visualized at 40× magnification under an optical microscope (Olympus BX60, Model BX60F5, and Olympus Optical Co., Ltd., Japan) equipped with a color VGA camera (Sony, Model no. SSC-DC- 58AP, Japan).[14]

Molecular Docking Studies. EGCG, HSA, and MINP Preparation. PubChem (https://pubchem.ncbi.nlm.nih.gov) was used to obtain the skeletal structures of EGCG and Fe in spatial data file format and then converted to Protein Data

https://doi.org/10.1021/acsomega.3c05743
ACS Omega 2023, 8, 48775−48786

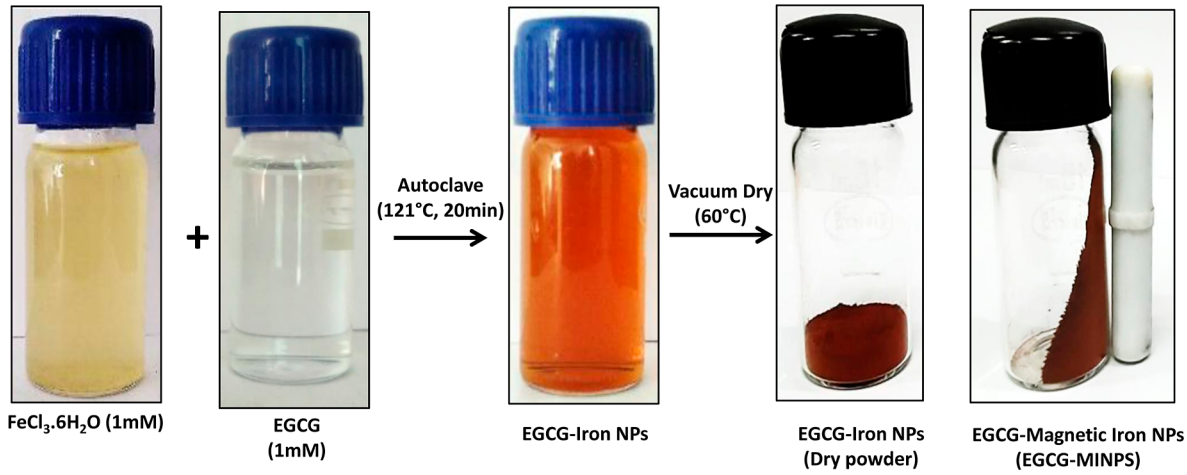

Figure 1. Schematic representation of the steps involved in the formation of EGCG-MINPs.

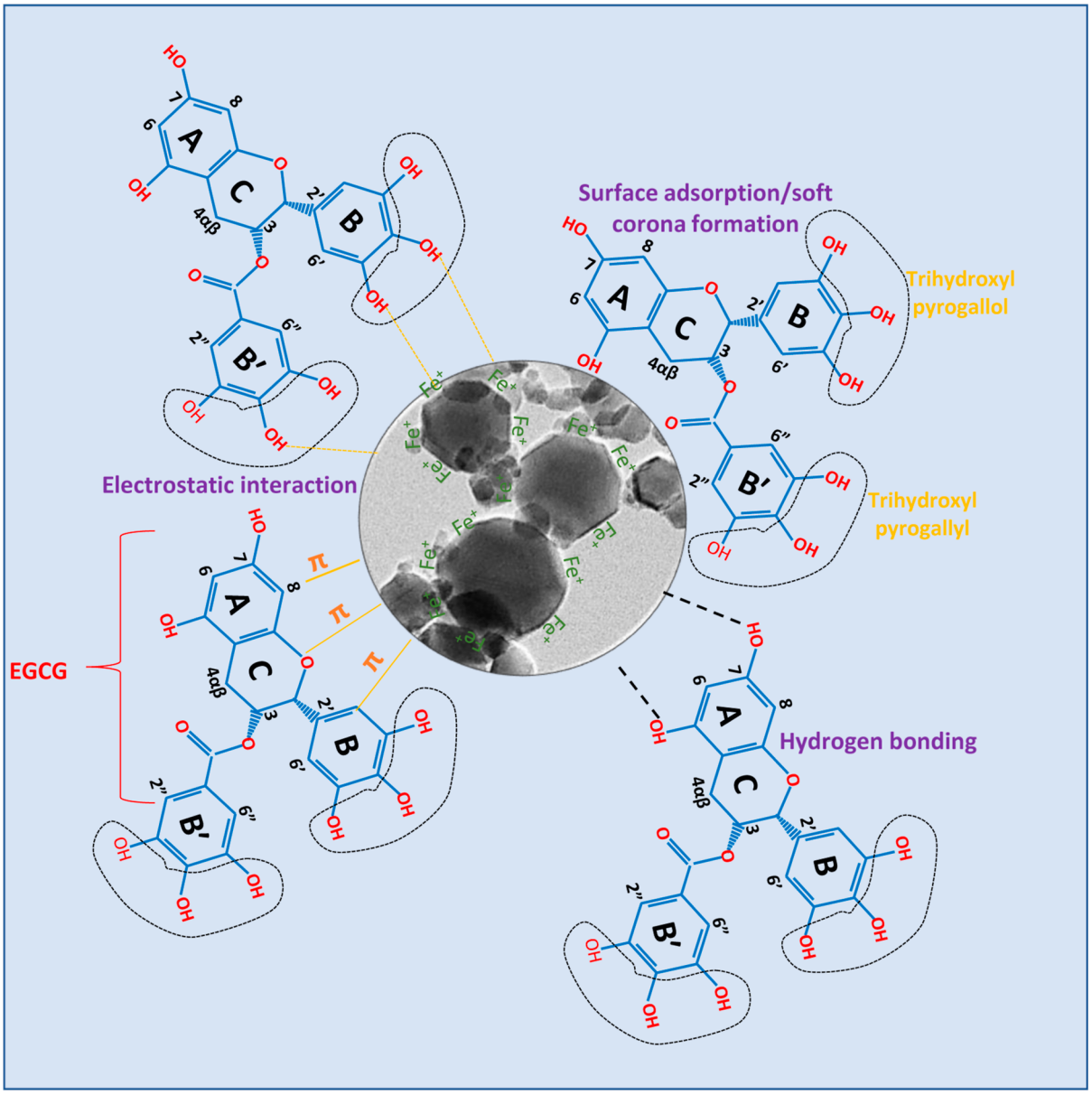

Figure 2. Possible mechanism of EGCG capping around magnetic EGCG-MINPs during NP synthesis.

https://doi.org/10.1021/acsomega.3c05743
ACS Omega 2023, 8, 48775−48786

Bank (PDB) format by using Chimera, an interaction visualizing program. Finally, EGCG and Fe were optimized and constructed in Marvin sketch and AutoDock Tools 4.2 software,[32] respectively. The 3D structure of HSA with PDB ID 7DZN was obtained from PDB (www.rcsb.org). Due to the interference in docking and development of complications in binding affinity calculations, the crystal water and HETATMs (*e.g.*, nonstandard/polar groups and coordinates) were deleted from the HSA structure.[33] For the molecular electrostatic potentialanalysis, Kollman charges and polar hydrogen atoms were added. During analysis, the overall energy was minimized by using Swiss PDB viewer.[34]

Docking Studies. First, we investigated the interactions that can develop between free EGCG and HSA by using the AutoDock 4.2 tool. Similarly, the interactions between the EGCG corona developed around our EGCG-MINPs and HSA were also assessed. Finally, we tested the hypothesis, that is, the slow release of free ionic Fe from the EGCG-MINPs in blood and their interactions with HSA. The grid map was set to 126 × 126 × 126, with the spacing of 0.375 Å for accuracy. Lastly, the simulation was performed using default genetic algorithm parameters, and 10 runs were generated for the ligand. Furthermore, the structure was visualized using Discovery Studio Visualizer.

Statistical Analysis. Data were expressed as mean ± SD for the values obtained from at least two independent experiments done in triplicate. Statistical analysis was performed by one-way analysis of variance (ANOVA) using the Holm−Sidak method, multiple comparisons versus the control group (Sigma Plot 11.0, USA). The level of statistical significance chosen was $^{*}p < 0.05$, unless otherwise stated.

RESULTS AND DISCUSSION

Synthesis of EGCG-MINPs. The biosynthesis of EGCG-MINPs was optimized by manipulating the pH of reaction mixtures. The nucleation of ionic Fe^{3+} into the active nuclei (Fe^{0}) of iron NPs was indicated by the change of reaction mixture into a brownish red color after three times heating process in an autoclave (121 °C and 15 psi pressure) (Figure 1).[4]

Recently, the study of Ali *et al.*[9] has shown that the vicinal trihydroxyl pyrogallol and galloyl moieties of EGCG were endowed with the intrinsic ability to chelate metal cations in order to reduce them into NPs. Specifically, the galloyl groups of EGCG can be speculated to get involved readily to form a stable metal phenolic network by developing hydrogen, cation−π, and $\pi-\pi$ interactions during EGCG-MINP formation (Figure 2).[28,35,36]

Briefly, during the reduction reaction, free EGCG and Fe^{3+} ions may react to create nucleation centers which eventually resulted in MINP formation.[37] Further, the surface absorption of EGCG on nascent MINPs by supramolecular interactions, viz., hydrogen bonding,[38] ionic interaction,[39] $\pi-\pi$ interactions, host−guest interaction, or reversible bond formation (*e.g.*, based on the Diels−Alder reaction),[40] provided the stability to the EGCG-MINPs.

Nevertheless, as-prepared aqueous solutions of EGCG-MINPs at pH 3.0, 5.0, 7.0, 9.0, and 11.0 were then collected in 50 mL conical centrifuge tubes. All independent mixtures were then spun at 5000 rpm for 5 min, and the pellets were dried. The as-prepared dry powder of EGCG-MINPs showed magnetic behavior against the magnetic bar, as shown in Figure 1. Finally, the powder EGCG-MINPs were stored in airtight vials to determine their physicochemical characteristics and antibacterial potential.

UV−Vis, DLS, and Zeta-Potential Analyses of EGCG-MINPs. The optical property of the as-prepared EGCG-MINPs is measured by UV−vis spectral analysis, as shown in Figure 3. The powder EGCG-MINPs, synthesized at pH 3.0, 5.0, 7.0, 9.0, and 11.0, were suspended (100 μg/mL) and sonicated (30% amplitude, 10 min) in deionized Milli-Q water for UV−vis, DLS-based hydrodynamic diameter, and zeta potential analyses. The results in Figure 3 exhibit the appearance of peaks centered around 409 nm in EGCG-MINP suspensions during the UV−vis spectroscopic analysis. Indeed, due to nanoscale confinement, the appearance of SPR in metal NPs indicates the collective oscillations of surface electrons in response to optical excitation.[41] However, broadening of peaks can be assigned to the decrease in crystal size.[42] The disappearance of peaks around 300 nm at alkaline pH can be speculated to be due to the accelerated interaction of free EGCG with nascent NPs while stabilizing the size as well as formation of soft corona of EGCG around EGCG-MINPs.[9] Indeed, compared to acidic pH, the structural stability of the EGCG skeleton and armed trihydroxyl pyrogallol and galloyl moieties is higher at alkaline pH, and thus an accelerated interaction between EGCG and Fe ions was speculated during the formation of EGCG−Fe complex or nascent NPs to stabilize the growth of particles.[9]

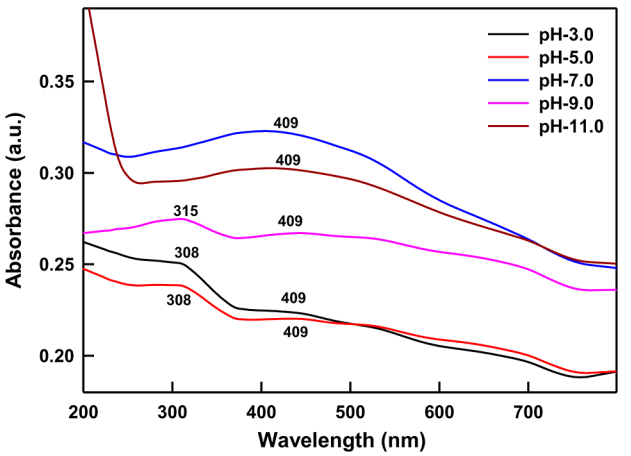

Figure 3. UV−vis spectra-based optimization of EGCG-MINP synthesis as a function of reaction pH (3.0, 5.0, 7.0, 9.0, and 11.0).

The histogram data in Figure 4A−E and Table 1 demonstrate the secondary or hydrodynamic size, PDI, and zeta potential of EGCG-MINPs dispersed in Milli-Q water. The DLS and PDI analyses of nanosuspensions revealed that the hydrodynamic size and PDI of EGCG-MINPs ranged 500−1062 nm and 0.299−0.527; however, the least hydrodynamic size and PDI were recorded in EGCG-MINPs synthesized at pH 5.0. However, the zeta potential of EGCG-MINPs was recorded in the range of −2.12 to −21.4 mV [Figure 4A(ii)−E(ii)].

Physicochemical Characterization of EGCG-MINPs. Briefly, among five EGCG-MINP formulations, the nanopowder obtained at pH 5.0 was considered for investigation, by employing the state-of-the-art techniques,[28] due to its smallest hydrodynamic size and high PDI. Both, FE-SEM [Figure 5A(i),(ii)]- and TEM [Figure 5B(i),(ii)]-based morphological analyses have witnessed the formation of pleomorphic EGCG-

https://doi.org/10.1021/acsomega.3c05743
ACS Omega 2023, 8, 48775−48786

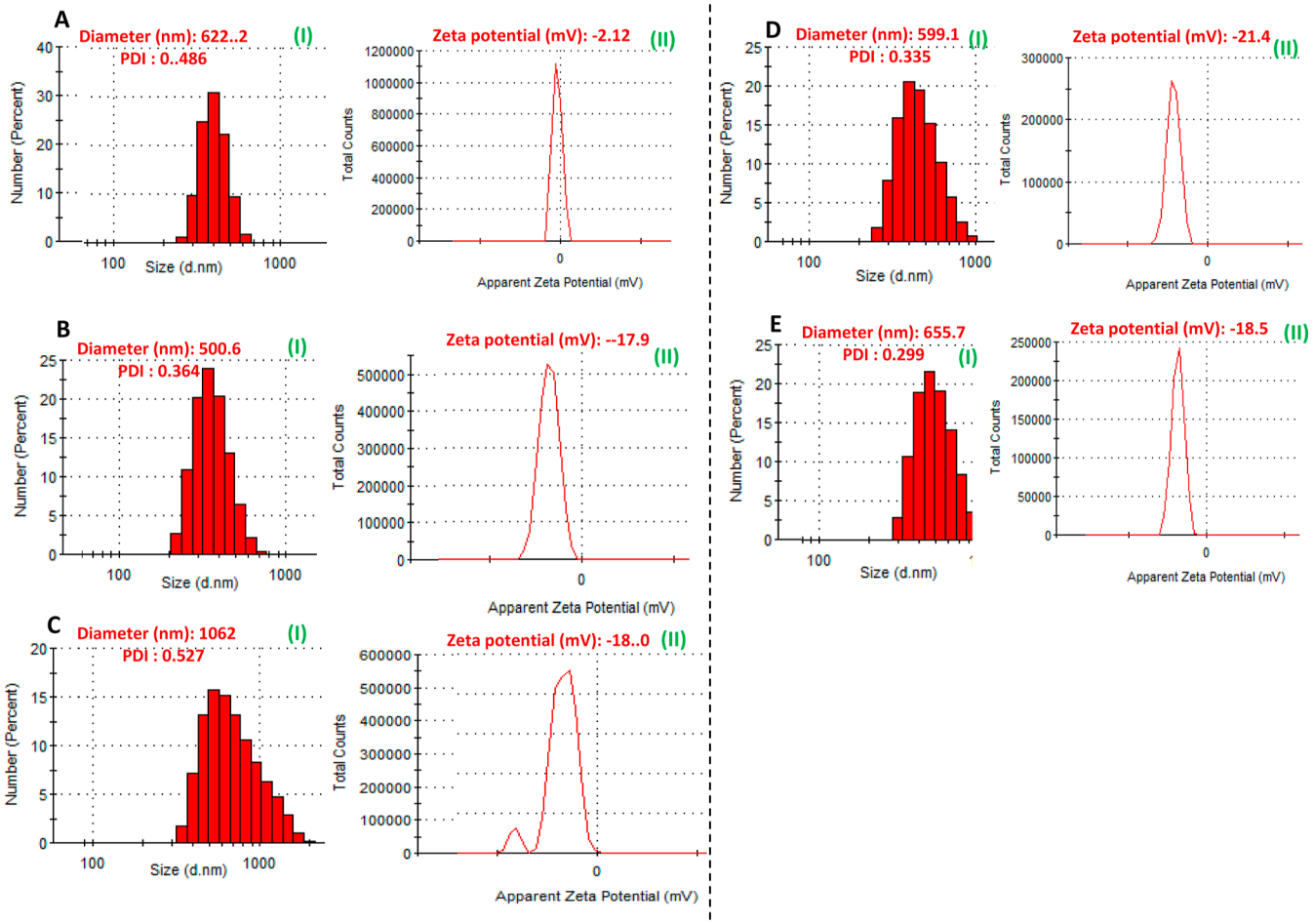

Figure 4. DLS-based size, PDI, and zeta potential analyses of EGCG-MINPs synthesized at pH 3.0 (A), 5.0 (B), 7.0 (C), 9.0 (D), and 11.0 (E).

Table 1. Size Stability, Surface Charge, and Dispersity of EGCG-MINPs at Different pH

S. no.	EGCG-MINPs	DLS (nm)	zeta-potential (mV)	PDI
1	pH 3	622.2 ± 62	−1.033 ± 0.25	0.486
2	pH 5	500.6 ± 87	−17.9 ± 0.05	0.364
3	pH 7	1062 ± 384	−18.16 ± 0.11	0.527
4	pH 9	599.1 ± 133	−21.56 ± 0.37	0.335
5	pH 11	655.7 ± 124	−18.46 ± 2.8	0.299

MINPs at pH 5.0. However, a majority of EGCG-MINPs exhibited well-grown and dispersed spherical and hexagonal shaped particles. Besides, ImageJ software-based analysis of FE-SEM [Figure 5A(i) and TEM (Figure 5B(i)] micrographs suggested that the average size of EGCG-MINPs ranged between 6.20 ± 0.08 [Figure 5B(iii)] and 9.73 ± 0.4 nm [Figure 5A(iii)]. The dispersity, shape, and precise size range of EGCG-MINPs were plausibly attributed to the soft corona of EGCG around NPs during the nucleation and stabilization in synthesis.[9]

FTIR-Based Characterization of EGCG-MINPs. The FTIR spectrum in Figure 6A exhibits the presence of the EGCG corona on EGCG-MINPs. The FTIR data supported the participation of EGCG moieties in EGCG-MINP formation by reflecting the vibrational, stretching, and bending signatures of EGCG functional groups. The FTIR outcomes also advocate that the as-synthesized EGCG-MINPs were metal oxide NPs, strongly due to the prominent vibrational signals appearing at 639, 560, 480, 442, and 420 cm^{-1}, which can readily be assigned to Fe ↔ O intrinsic stretching vibration, Fe−O deformation, Fe−O−Fe bending, and metal−oxygen (*i.e.*, Fe−O) complex stretching in octahedral and tetrahedral sites.[28,39] Besides, the sharp band at 3414 cm^{-1} in the FTIR spectrum of EGCG-MINPs also indicated that the OH-bearing EGCG compound has participated actively in the reduction of Fe^{3+} ions during nucleation and NP formation. The signals ascribed to aliphatic CH and CH_2, CH stretching of alkenes and C═O stretch of amide-I at 2918, 2834, and 1631 cm^{-1}, respectively, can be argued to be attributed to or formed by NaOH and HCl used to stabilize the pH of reactions (Table 2).

Purity and Crystallinity Analyses of EGCG-MINPs. X-ray diffraction (XRD) is a promising technique that can yield decisive structural information including phase identification, crystallinity, and average crystal size of the nanomaterial under investigation. All peaks of the EGCG-MINP XRD patterns were unambiguously indexed to the α-Fe_2O_3NPs lattice phase and *hkl* planes at 2-theta positions as 104, 201, 116, 206, 216, and 109 and matched with the JCPDS card no. 84-308 (with the referenced lattice constant a = 5.0356 Å, c = 13.7489 Å, and c/a = 2.7303.[39,40] The diffraction patterns indicated the formation of a rhombohedrally centered hexagonal structure of EGCG-α-Fe_2O_3NPs (*i.e.*, EGCG-MONPs).[41] The average diameter (16.7 nm) of EGCG-MINPs was calculated with the full width at half-maximum (fwhm) value of (201) Bragg reflection[42] by using Scherrer's formula.

https://doi.org/10.1021/acsomega.3c05743
ACS Omega 2023, 8, 48775−48786

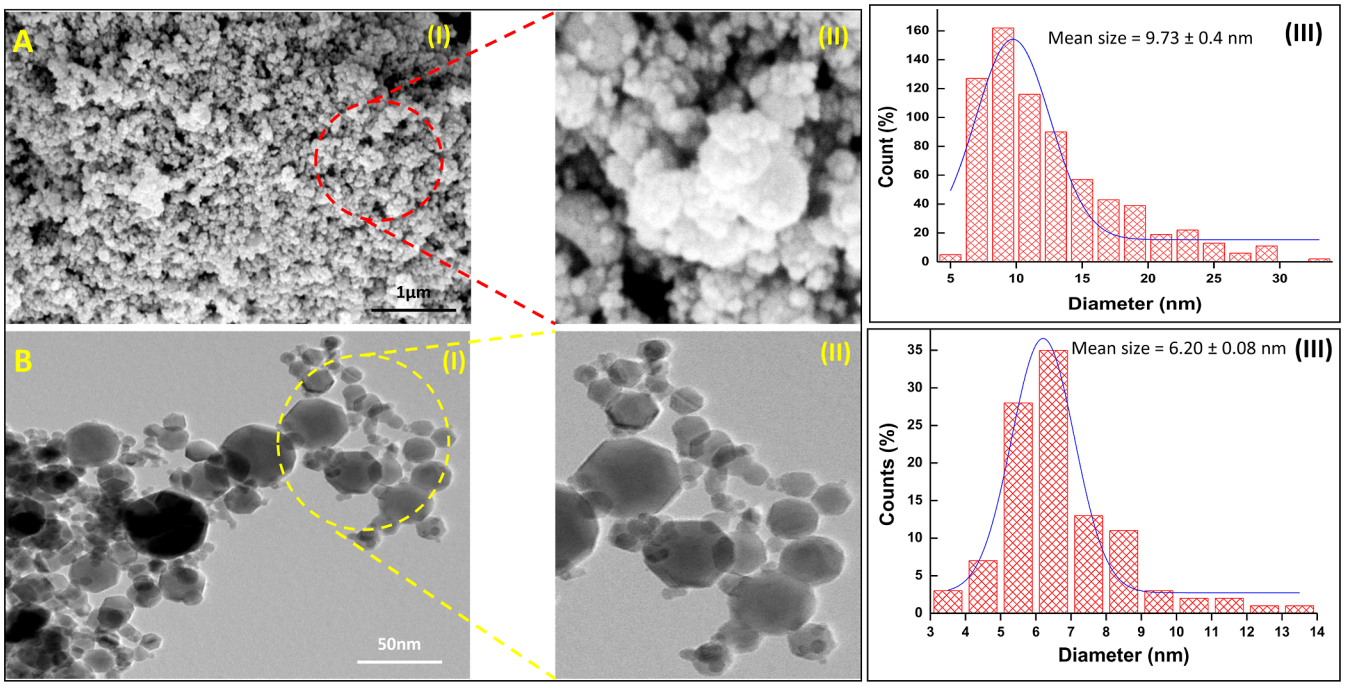

Figure 5. Comparative analysis of morphologies and sizes of EGCG-MINPs synthesized at pH −5 by FE-SEM (A i,ii) and TEM (B i,ii). Panels A iii and B iii represent ImageJ-based size distribution as well as the average size of EGCG-MINPs demonstrated in the FE-SEM and TEM micrographs.

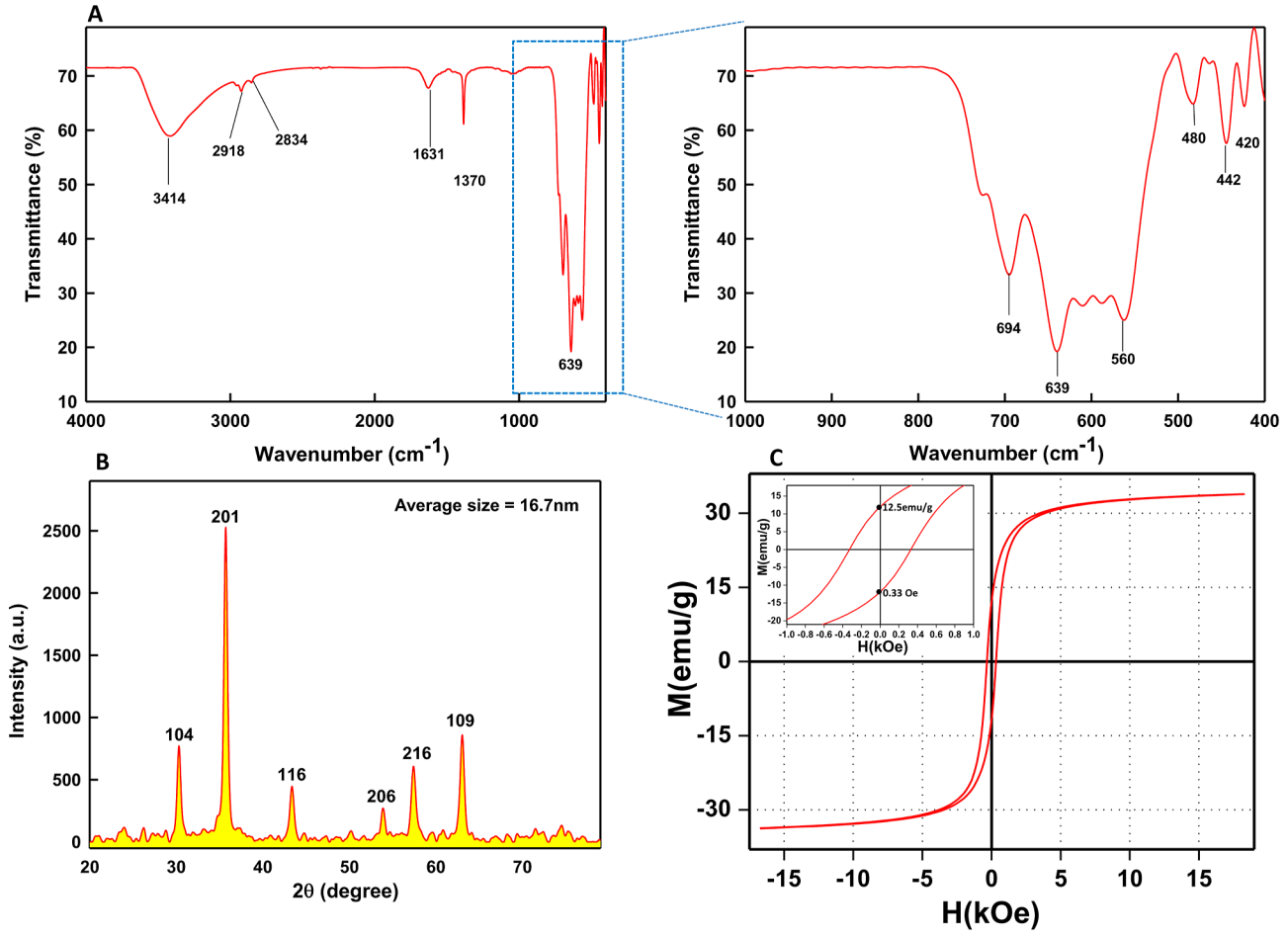

Figure 6. (A) FTIR spectra of EGCG-MINPs. (B) XRD analysis. (C) VSM image of the synthesized EGCG-MINPs at pH 5. Inset shows the hysteresis magnetic loop of EGCG-MINPs.

https://doi.org/10.1021/acsomega.3c05743
ACS Omega 2023, 8, 48775−48786

Table 2. FTIR Analysis of EGCG-MINPs

S. no.	wave number (cm^{-1})	bond assignments	references
1	3414	O−H stretching of carbohydrates and alcohol	4
2	2918	CH and CH_2 stretching of aliphatic group	9
3	2834	CH stretching of alkenes	15
4	1631	C═O stretch of amide I	4
5	1370	CH bending of methyl group	14
6	694	C−H vibrations in aromatic compound	14
7	639	intrinsic stretching vibration of Fe ↔ O	4
8	560	Fe−O deformation in octahedral and tetrahedral sites	4
9	480	Fe−O−Fe bending vibration in octahedral site	4
10	442	Fe−O−Fe bending vibration in octahedral site	42
12	420	metal−oxygen complex stretching	42

Magnetic Behavior of EGCG-MINPs. Indeed, most of the iron oxides are well-known magnetic materials, including α-Fe_2O_3. Hence, we measured the magnetic hysteresis of the as-prepared EGCG-MINPs on a VSM. The data presented in Figure 6C exhibit that the hysteresis loop did not meet saturation even at the maximum magnetic field. The enlarged inset in Figure 5C suggests that the magnetization property of EGCG-MINPs shows a hysteretic feature with 33.64, 12.18, and 0.33 Oe of saturation magnetization (Ms), remanent magnetization (Mr), and coercivity (Hc), respectively. Beyond, the high M_r value of 12.18 emu/g can be ascribed to the hexagonal shape, whereas the low Hc value of 0.33 Oe was likely due to the nanoscale size of EGCG-MINPs.[43] Owing to such promising magnetic properties, the as-prepared EGCG-MINPs can be envisaged as successful antibacterial carriers for instant deeper penetration and homogeneous distribution across multicomponent biofilm matrices by external magnetic field stimulation.[44]

Antibacterial Potential of EGCG-MINPs against Bacterial Isolates. The as-synthesized EGCG-MINPs were assessed for their antibacterial and antibiofilm activities against Gram-negative NDM-1-producing bacteria. The data in Table 3 demonstrate that at 1000 μg/mL of EGCG-MINPs, based on

Table 3. Determination of the MICs and MBCs of EGCG-MINPs against Test Bacteria

bacterial strains	EGCG-MINPs (μg/mL)	
	MIC (survival %)	MBC
E. coli (AK-33)	>1000 (34.59%)	2000
K. pneumoniae (AK-65)	1000 (17.88%)	2000
P. aeruginosa (AK-66)	>1000 (35.36%)	2000
S. boydii (AK-67)	>1000 (38.55%)	2000

$OD_{600\ nm}$, the survival percent of *E. coli*, *K. pneumoniae*, *P. aeruginosa*, and *S. boydii* was estimated as 34.59, 17.88, 35.36, and 38.55%, respectively, compared to untreated control experiments (*i.e.*, 100%). Importantly, >80% decline in the survival of microorganisms against antimicrobials can be considered as its MIC value, whereas ∼ 100% reduction can be marked as the MBC value. Nevertheless, in the present study, the MICs of EGCG-MINPs against *E. coli*, *P. aeruginosa*, and *S. boydii* can be considered as >1000 μg/mL, whereas the MIC value against *K. pneumoniae* was determined to be 1000 μg/mL. Under identical conditions, the data also suggest that the sensitivity pattern of the test bacteria against EGCG-MINPs was as follows: *K. pneumoniae* > *E. coli* > *P. aeruginosa* > *S. boydii* (Table 3). Beyond this, the differential trend of sensitivity against EGCG-MINPs was also investigated in parallel by comparing the cellular damage in augmented EGCG-MINP-treated *E. coli*, *K. pneumoniae*, *P. aeruginosa*, and *S. boydii* cells. The SEM micrographs shown in Figure 7

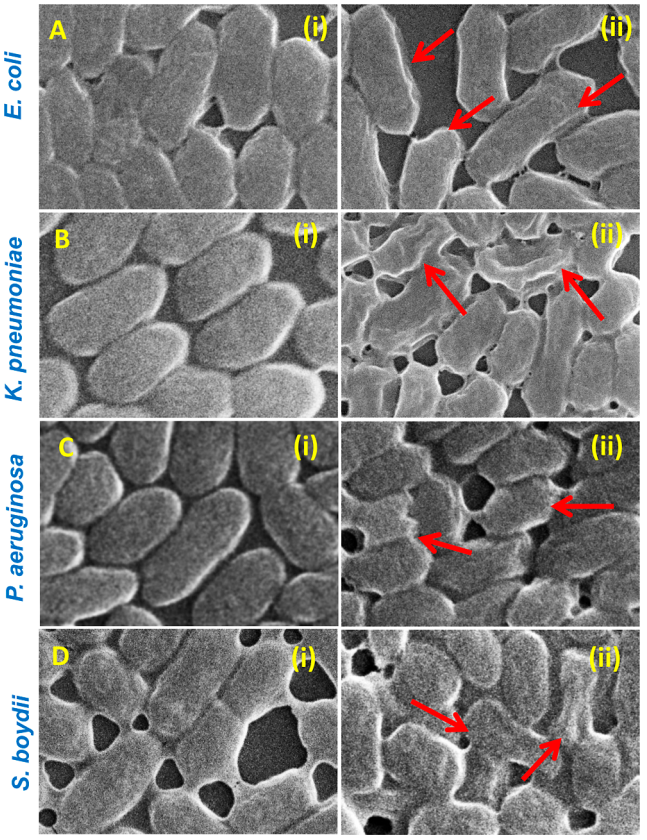

Figure 7. Representative SEM micrographs of untreated control (i); EGCG-MINP-treated (ii) NDM-1-producing cells of *E. coli* (A), *K. pneumoniae* (B) *P. aeruginosa* (C), and *S. boydii* (D).

evidently confirm the antibacterial potential of EGCG-MINPs. Compared to untreated control panels [Figure 7A(i)−D(i)], there were severe morphological damages, such as the loss of native shape and size, broken cell wall, and formation of pits and cavities in the treated *E. coli*, *K. pneumoniae*, *P. aeruginosa*, and *S. boydii* cells [Figure 7A(ii)−D(ii)]. However, among the four treated Gram-negative bacteria, cells of *K. pneumoniae* were noticed to be the most damaged [Figure 7B(ii)].

Antibiofilm Activities of EGCG-MINPs. The clinical management of biofilm-producing bacteria is often more challenging than that of nonbiofilm producers, due to the poor access of antimicrobials through the biofilm matrix to target bacterial cells. Besides, due to antibiotic inefficacy, the successful treatment of biofilm-associated chronic infections becomes more complicated when the prevalence of ESβL and NDM-1 producers is high in biofilms. Nevertheless, in this study, the Gram-negative NDM-1-positive as well as potential biofilm-producing test bacteria, *E. coli*, *K. pneumoniae*, *P. aeruginosa*, and *S. boydii* were investigated against the as-prepared EGCG-MINPs. The data in Figure 8 show significant ($p < 0.001$) biofilm inhibition. Concisely, the *E. coli*, *K.*

https://doi.org/10.1021/acsomega.3c05743
ACS Omega 2023, 8, 48775−48786

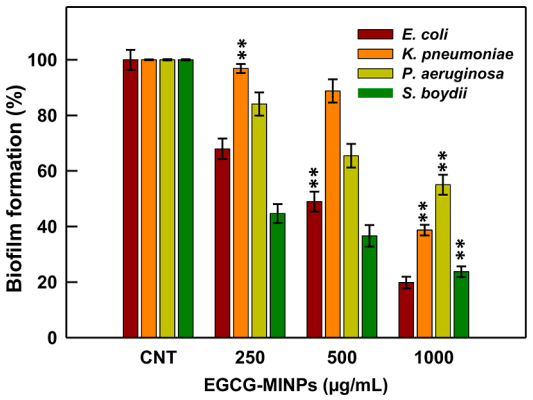

Figure 8. Dose-dependent inhibition of biofilm formation in *E. coli*, *K. pneumoniae*, *P. aeruginosa*, and *S. boydii* under 0−1000 μg/mL stress of EGCG-MINPs. Error bars represent the mean ± SD of three independent experiments performed in triplicate. Asterisks denote significant difference at $*p < 0.001$ and $**p < 0.05$ determined by one-way ANOVA, followed by the Holm−Sidak method for multiple comparisons.

pneumoniae, *P. aeruginosa,* and *S. boydii* cells treated with EGCG-MINPs in the concentration range of 250−1000 μg/mL inhibited the biofilm formation by 32.06 ± 3.7 to 80.16 ± 2.0, 3.13 ± 1.6 to 61.30 ± 1.8, 15.91 ± 4.1 to 44.97 ± 3.5, and 55.33 ± 3.3 to 76.27 ± 1.9%, respectively, as compared to the untreated control experiments (Figure 8).

The obtained biofilm inhibitory trends suggested that EGCG-MINPs can be a viable option while managing the biofilm-associated bacterial infections. At the same time, it can be envisaged that the released Fe^{3+} ions from EGCG-MINPs were readily chelated by the biofilm biomolecules like enzymes, proteins, and organic acids (*i.e.*, eDNA, eRNA, EPS, *etc.*), which ultimately resulted in attenuated quorum sensing and degradation of the biofilm.[41] It can also be argued that, compared to bare metallic NPs, the soft biological corona of EGCG around MINPs enhanced the (i) dispersity of nanostructures, (ii) stability in harsh acidic niches, and (iii) surface contact killing of bacteria embedded in a dense biofilm. Our microscopic studies have also apparently supported the dose-dependent biofilm inhibitory potential of EGCG-MINPs. The representative micrographs in Figure 9A(ii)−D(iv) have demonstrated a dose-dependent reduction in biofilm formation.

Docking Outcomes. EGCG, a polyphenolic catechin, has been reported as the most abundant (∼95%) multifunctional polyphenol in traditional brewed green tea.[9] Similarly, HSA, are the most abundant soluble proteins of the circulatory system, importantly known to carry numerous exo- and endogenous compounds including drugs, ligands, fatty acids, metal ions, amino acids, steroids, and so forth.[44] At the other end, ionic iron species, *i.e.*, Fe^{3+}, has also been witnessed to play several crucial physiological roles in almost all living organisms, including hemoglobin formation and oxygen delivery.[45,46] Also, the strong binding of albumin to the drug enhances its *in vivo* half-life while decreasing the bioavailability and *vice versa*.[47] Thus, specifically in biomedical and pharmaceutical research areas, research on the interactional behavior of HSA toward modern synthesized drug compounds or formulations has become a hot field of interest.[48]

Further, in the NP-based drug delivery system, the nanodrugs or nanoparticles administered in the bloodstream instantly interact with the surrounded plasma proteins and get encapsulated with a soft corona of protein.[49] This further surface modification of nanodrugs may enhance the interaction with specific target cells. Thus, such nonspecific interactions of

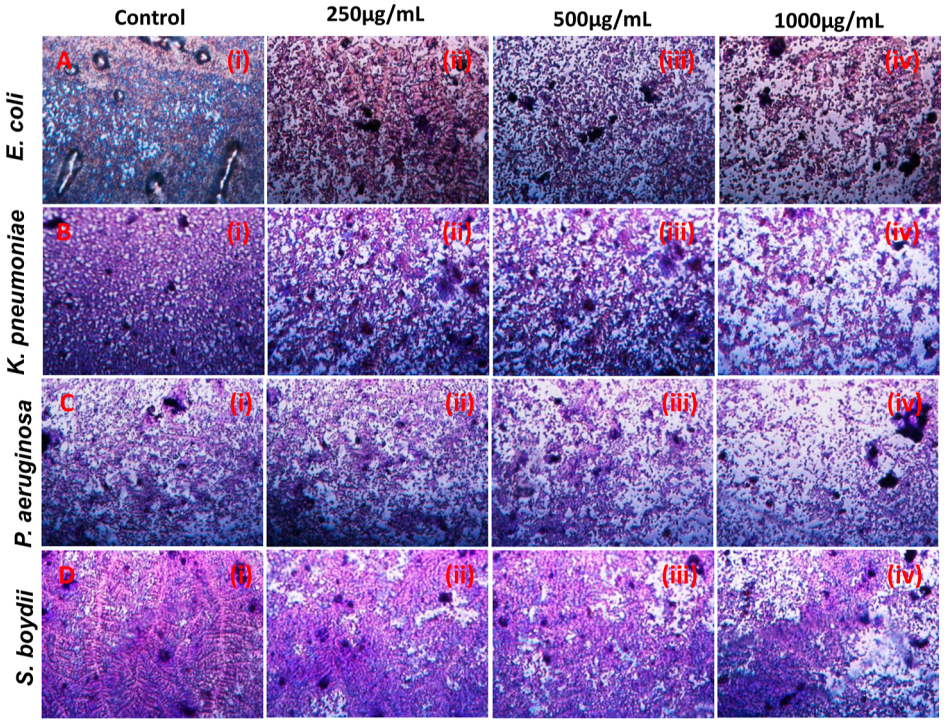

Figure 9. Inhibition of *E. coli* (A), *K. pneumoniae* (B), *P. aeruginosa* (C), and *S. boydii* (D) biofilm formation by EGCG-MINP-treated NDM-1 isolates. Panels show the biofilm micrographs as (i) untreated control and experiments treated with 250 (ii), 500 (iii), and 1000 μg/mL (iv) of EGCG-MINPs.

https://doi.org/10.1021/acsomega.3c05743
ACS Omega 2023, 8, 48775−48786

Table 4. Molecular Docking Results

S. no.	HSA−ligand[a] interaction	binding affinity (kcal/mol)	estimated inhibition constant (ki) in nm	internal energy (kcal/mol)	no. of H bonds	amino acid residues
1.	EGCG-HSA	−8.28	84.92	−5.07	1	Glu542, Lys541, Glu542, Thr540, Lys 538, Val 493, Glu492, Lys413, Val409, Ala406, Arg410, Lys414, Leu491, Ser489, Asn405
2.	Fe-HSA	−9.15	36.45	−5.32	2	Gln390, Asn386, Leu387, Glu382, Glu383, Pro379, Leu380, Ser489, Lys414, Ala490, Ala539, Lys539, Lys 538, Pro537, Pro499
3.	(Fe-EGCG)- HSA	−11.78	102.80	−3.97	1	Lys541, Glu442, Glu542, Lys413, Thr540, His242, Lys538, Ala539, Thr540, Glu542, Arg410

[a]=EGCG alone, Fe alone, and Fe−EGCG complex.

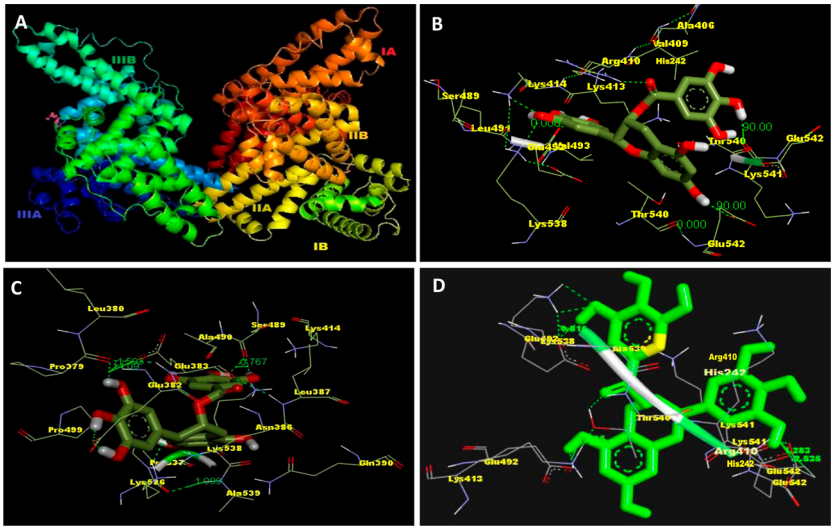

Figure 10. (A) Stereo view of HSA showing all three domains. (B) Active site residues of HSA and EGCG. (C, D) Active site residues of HSA and Fe, and HSA and EGCG−Fe complex, using Discovery Studio Visualizer.

drug carrier NPs eventually lose selectivity for the targeted drug delivery system. Nevertheless, in the present study, we strived to test our hypothesis, *in silico*, what if the as-synthesized EGCG-MINP formulation was injected in the bloodstream, to explore the HSA interactional behaviors toward the EGCG-MINPs or released EGCG and Fe constituents. For this, molecular docking study is the most convincing strategy to understand the interactional behaviors of proteins. Concisely, the results in Table 4 exhibit an apparent pattern of increase in the binding energy of HSA as −8.28, −9.15, and −11.78 kcal/mol toward free EGCG, Fe and Fe−EGCG complex, or EGCG-MINPs, respectively.

The highest binding affinity (−11.78 kcal/mol) between HSA and Fe−EGCG complex is likely due to the involvement of 11 amino acids, namely, Lys541, Glu442, Glu542, Lys413, Thr540, His242, Lys538, Ala539, Thr540, Glu542, and Arg410. Besides, the presence of hydrophobic side chains lining over the inner side and positively charged amino acids at the entrance of the domain can be speculated as the primary reason for the greatest binding affinity of the Fe−EGCG complex (Figure 10A−D).

Besides, the binding interaction visualization demonstrated the involvement of these amino acid residues in 2D conformational interactions through establishing hydrogen bonds within the subdomain IIA cavity, as shown in the study of Sekar *et al.*[50] Besides, the number of hydrophobic, polar, nonpolar, and hydrogen bonds, formed during protein and ligand interaction, represented the total internal energy taken. According to Dong *et al.*,[51] the change in affinities largely relies on noncovalent bonds along with auxiliary molecules. The interaction between a ligand and protein can trigger positive electrostatic energy generation, which hinders the binding mechanism. However, in the present study, initial interactions of HSA with ligands EGCG alone, Fe alone, and EGCG−Fe complex yielded negative internal energies of −5.07, −5.32, and −3.97 kcal/mol, respectively, which in fact warranted an easier and stable interaction (Table 4). Overall, the results herein indicate clearly that surface modification of metallic NPs with bioactive plant polyphenol molecules can (i) facilitate the interaction between HSA and metallic NPs, (ii) stabilize the HSA−NP complex, and (iii) thus increase the drug payload delivery in metallic NP-based injectable drug delivery system.

CONCLUSIONS

This study demonstrated an efficient, facile, moist-heating (*e.g.*, autoclave), one-step procedure for pH-dependent green synthesis of narrow-sized magnetic iron oxide NPs (α-Fe_2O_3NPs) using aqueous EGCG and $FeCl_3$ as reducing/stabilizing agents and iron source, respectively. The characterization of the as-synthesized EGCG-capped magnetic iron oxide α-Fe_2O_3NPs (EGCG-MINPs) revealed the formation of pleomorphic magnetic nanostructures with a majority of spherical and hexagonal shapes in the primary size range of 6.20−16.7 nm. However, the DLS-based secondary size, PDI, and surface potential were recorded in the range of 500−1062

https://doi.org/10.1021/acsomega.3c05743
ACS Omega 2023, 8, 48775−48786

nm, 0.299−0.527, and 2.12 to −21.4 mV, respectively. The FTIR results have confirmed the involvement of EGCG in reduction and fabrication of Fe^{3+} ions to EGCG-MINPs. The VSM analysis confirmed that EGCG-MINPs possess an excellent magnetic feature. Dose-dependent antibacterial and antibiofilm activities against Gram-negative NDM-1-producing *E. coli*, *K. pneumoniae*, *E. aeruginosa*, and *S. boydii* bacterial cells were likely due to EGCG surface corona-facilitated penetration of EGCG-MINPs into bacterial cells as well as the released Fe^{3+} ion-mediated disruption of quorum sensing biomolecules. In addition, molecular docking experiments revealed that compared to free Fe^{3+} and EGCG alone, the EGCG-MINPs or Fe−EGCG complex possess a significantly high binding affinity toward HSA and hence can be considered as promising biocompatible nanodrug carriers in *in vivo* drug delivery systems.

AUTHOR INFORMATION

Corresponding Author

Asad U. Khan − *Medical Microbiology and Molecular Biology Laboratory, Interdisciplinary Biotechnology Unit, Aligarh Muslim University, Aligarh 202002 UP, India*; orcid.org/0000-0001-9191-9423; Email: asadukhan72@gmail.com

Authors

Khursheed Ali − *Medical Microbiology and Molecular Biology Laboratory, Interdisciplinary Biotechnology Unit, Aligarh Muslim University, Aligarh 202002 UP, India*

Shruti Rakesh − *Medical Microbiology and Molecular Biology Laboratory, Interdisciplinary Biotechnology Unit, Aligarh Muslim University, Aligarh 202002 UP, India*

Shamsi Khalid − *Medical Microbiology and Molecular Biology Laboratory, Interdisciplinary Biotechnology Unit, Aligarh Muslim University, Aligarh 202002 UP, India*

Complete contact information is available at: https://pubs.acs.org/10.1021/acsomega.3c05743

Notes

The authors declare no competing financial interest.

ACKNOWLEDGMENTS

We acknowledge the Department of Biotechnology grant no. **BT/PR40148/BTIS/137/20/2021 and Indian Council of Medical Research no: 35/08/2022-Nano/BMS**. This work was performed at The Department of Interdisciplinary Biotechnology Unit, Aligarh Muslim University, India. The materials characterization and the Biosciences and Electron Microscopy facilities were availed at University Sophisticated Instrumentation Facilities (USIF).

REFERENCES

(1) Hais, R. U. o.; Amr, S. o.; Team, A.-I.; Tomczyk, S.; Zanuzdana, A.; Heck, A.; Haller, S.; Abu Sin, M.; Eckmanns, T. *European Centre for Disease Prevention and Control (ECDC)*, 2022.

(2) Yong, D.; Toleman, M. A.; Giske, C. G.; Cho, H. S.; Sundman, K.; Lee, K.; Walsh, T. R. Characterization of a new metallo-β-lactamase gene, bla NDM-1, and a novel erythromycin esterase gene carried on a unique genetic structure in Klebsiella pneumoniae sequence type 14 from India. *Antimicrobial agents and chemotherapy.* **2009**, *53* (12), 5046−5054.

(3) Beg, A. Z.; Khan, A. U. Exploring bacterial resistome and resistance dessemination: an approach of whole genome sequencing. *Future Med. Chem.* **2019**, *11* (3), 247−260.

(4) Ali, K.; Ahmed, B.; Khan, M. S.; Musarrat, J. Differential surface contact killing of pristine and low EPS Pseudomonas aeruginosa with Aloe vera capped hematite (α-Fe2O3) nanoparticles. *Journal of Photochemistry and Photobiology B: Biology.* **2018**, *188*, 146−158.

(5) Qayyum, S.; Khan, A. U. Nanoparticles vs. biofilms: a battle against another paradigm of antibiotic resistance. *MedChemComm.* **2016**, *7* (8), 1479−1498.

(6) Chung, K. K.; Schumacher, J. F.; Sampson, E. M.; Burne, R. A.; Antonelli, P. J.; Brennan, A. B. Impact of engineered surface microtopography on biofilm formation of Staphylococcus aureus. *Biointerphases.* **2007**, *2* (2), 89−94.

(7) Ma, P. A.; Xiao, H.; Yu, C.; Liu, J.; Cheng, Z.; Song, H.; Zhang, X.; Li, C.; Wang, J.; Gu, Z.; et al. Enhanced cisplatin chemotherapy by iron oxide nanocarrier-mediated generation of highly toxic reactive oxygen species. *Nano Lett.* **2017**, *17* (2), 928−937.

(8) Zhu, K.; Deng, Z.; Liu, G.; Hu, J.; Liu, S. Photoregulated cross-linking of superparamagnetic iron oxide nanoparticle (spion) loaded hybrid nanovectors with synergistic drug release and magnetic resonance (MR) imaging enhancement. *Macromolecules* **2017**, *50* (3), 1113−1125.

(9) Ali, K.; Zaidi, S.; Khan, A. A.; Khan, A. U. Orally fed EGCG coronate food released TiO2 and enhanced penetrability into body organs via gut. *Biomater. Adv.* **2023**, *144*, 213205.

(10) Ali, K.; Saquib, Q.; Siddiqui, M. A.; Ahmad, J.; Al-Khedhairy, A. A.; Musarrat, J. Anti-cancer efficacy of Aloe vera capped hematite nanoparticles in human breast cancer (MCF-7) cells. *J. Drug Delivery Sci. Technol.* **2020**, *60*, 102052.

(11) Ahmed, B.; Syed, A.; Ali, K.; Elgorban, A. M.; Khan, A.; Lee, J.; Al-Shwaiman, H. A. Synthesis of gallotannin capped iron oxide nanoparticles and their broad spectrum biological applications. *RSC Adv.* **2021**, *11* (17), 9880−9893.

(12) Ali, K.; Ahmed, B.; Ansari, S. M.; Saquib, Q.; Al-Khedhairy, A. A.; Dwivedi, S.; Alshaeri, M.; Khan, M. S.; Musarrat, J. Comparative in situ ROS mediated killing of bacteria with bulk analogue, Eucalyptus leaf extract (ELE)-capped and bare surface copper oxide nanoparticles. *Mater. Sci. Eng. C* **2019**, *100*, 747−758.

(13) Akhtar, F.; Khan, A. U.; Qazi, B.; Kulanthaivel, S.; Mishra, P.; Akhtar, K.; Ali, A. A nano phototheranostic approach of toluidine blue conjugated gold silver core shells mediated photodynamic therapy to treat diabetic foot ulcer. *Sci. Rep.* **2021**, *11* (1), 24464.

(14) Ali, K.; Dwivedi, S.; Azam, A.; Saquib, Q.; Al-Said, M. S.; Alkhedhairy, A. A.; Musarrat, J. Aloe vera extract functionalized zinc oxide nanoparticles as nanoantibiotics against multi-drug resistant clinical bacterial isolates. *J. Colloid Interface Sci.* **2016**, *472*, 145−156.

(15) Ali, K.; Ahmed, B.; Dwivedi, S.; Saquib, Q.; Al-Khedhairy, A. A.; Musarrat, J. Microwave accelerated green synthesis of stable silver nanoparticles with Eucalyptus globulus leaf extract and their antibacterial and antibiofilm activity on clinical isolates. *PLoS One* **2015**, *10* (7), No. e0131178.

(16) Fatima, S.; Ali, K.; Ahmed, B.; Al Kheraif, A. A.; Syed, A.; Elgorban, A. M.; Musarrat, J.; Lee, J. Titanium dioxide nanoparticles Induce inhibitory effects against planktonic cells and biofilms of human oral cavity isolates of Rothia mucilaginosa, Georgenia sp. and Staphylococcus saprophyticus. *Pharmaceutics.* **2021**, *13* (10), 1564.

(17) Geng, J.; Zhu, J. J.; Lu, D. J.; Chen, H. Y. Hollow PbWO4 nanospindles via a facile sonochemical route. *Inorg. Chem.* **2006**, *45* (20), 8403−8407.

(18) Geng, J.; Hou, W. H.; Lv, Y. N.; Zhu, J. J.; Chen, H. Y. One-dimensional BiPO4 nanorods and two-dimensional BiOCl lamellae: fast low-temperature sonochemical synthesis, characterization, and growth mechanism. *Inorg. Chem.* **2005**, *44* (23), 8503−8509.

(19) Roh, H. S.; Potdar, H. S.; Jun, K. W.; Kim, J. W.; Oh, Y. S. Carbon dioxide reforming of methane over Ni incorporated into Ce−ZrO2 catalysts. *Appl. Catal., A* **2004**, *276* (1−2), 231−239.

(20) Chanajaree, R.; Ratanatawanate, C.; Ruangchaithaweesuk, S.; Lee, V. S.; Wittayanarakul, K. Colorimetric detection of Pb2+ ions using curcumin silver nanoparticles. *J. Mol. Liq.* **2021**, *343*, 117629.

(21) Javadian, S.; Najafi, K.; Sadrpoor, S. M.; Ektefa, F.; Dalir, N.; Nikkhah, M. Graphene quantum dots based magnetic nanoparticles as

a promising delivery system for controlled doxorubicin release. *J. Mol. Liq.* **2021**, *331*, 115746.
(22) Amiri, M.; Akbari, A.; Ahmadi, M.; Pardakhti, A.; Salavati-Niasari, M. Synthesis and in vitro evaluation of a novel magnetic drug delivery system; proecological method for the preparation of CoFe2O4 nanostructures. *J. Mol. Liq.* **2018**, *249*, 1151−1160.
(23) Rufus, A.; Sreeju, N.; Vilas, V.; Philip, D. Biosynthesis of hematite (α-Fe2O3) nanostructures: Size effects on applications in thermal conductivity, catalysis, and antibacterial activity. *J. Mol. Liq.* **2017**, *242*, 537−549, DOI: 10.1016/j.molliq.2017.07.057.
(24) Chen, J.; Xu, L.; Li, W.; Gou, X. α-Fe2O3 nanotubes in gas sensor and lithium-ion battery applications. *Adv. Mater.* **2005**, *17* (5), 582−586.
(25) Allen, M.; Willits, D.; Mosolf, J.; Young, M.; Douglas, T. Protein cage constrained synthesis of ferrimagnetic iron oxide nanoparticles. *Adv. Mater.* **2002**, *14* (21), 1562−1565.
(26) Ahmmad, B.; Leonard, K.; Shariful Islam, M.; Kurawaki, J.; Muruganandham, M.; Ohkubo, T.; Kuroda, Y. Green synthesis of mesoporous hematite (α-Fe2O3) nanoparticles and their photocatalytic activity. *Adv. Powder Technol.* **2013**, *24* (1), 160−167.
(27) Ahmmad, B.; Kanomata, K.; Hirose, F.; Kurawaki, J.; Ohkubo, T. Biosynthesis of elliptical hematite microparticles and their photocatalytic performance. *Journal of Current Science and Technology.* **2014**, *4* (1), 31−38.
(28) Ali, K.; Abul Qais, F.; Dwivedi, S.; Abdel-Salam, E. M.; Ansari, S. M.; Saquib, Q.; Faisal, M.; Al-Khedhairy, A. A.; Al-Shaeri, M.; Musarrat, J. Titanium dioxide nanoparticles preferentially bind in subdomains IB, IIA of HSA and minor groove of DNA. *J. Biomol. Struct. Dyn.* **2018**, *36* (10), 2530−2542.
(29) Zhu, M.; Wang, Y.; Meng, D.; Qin, X.; Diao, G. Hydrothermal synthesis of hematite nanoparticles and their electrochemical properties. *J. Phys. Chem. C* **2012**, *116* (30), 16276−16285.
(30) Cherian, T.; Ali, K.; Fatima, S.; Saquib, Q.; Ansari, S. M.; Alwathnani, H. A.; Al-Khedhairy, A. A.; Al-Shaeri, M.; Musarrat, J. Myristica fragrans bio-active ester functionalized ZnO nanoparticles exhibit antibacterial and antibiofilm activities in clinical isolates. *J. Microbiol. Methods* **2019**, *166*, 105716.
(31) Cherian, T.; Ali, K.; Saquib, Q.; Faisal, M.; Wahab, R.; Musarrat, J. Cymbopogon citratus functionalized green synthesis of CuO-nanoparticles: Novel prospects as antibacterial and antibiofilm agents. *Biomolecules.* **2020**, *10* (2), 169.
(32) Morris, G. M.; Huey, R.; Lindstrom, W.; Sanner, M. F.; Belew, R. K.; Goodsell, D. S.; Olson, A. J. AutoDock4 and AutoDockTools4: Automated docking with selective receptor flexibility. *J. Comput. Chem.* **2009**, *30* (16), 2785−2791.
(33) Wong, S. E.; Lightstone, F. C. Accounting for water molecules in drug design. *Expert Opin. Drug Discovery* **2011**, *6* (1), 65−74.
(34) Guex, N.; Peitsch, M. C. SWISS-MODEL and the Swiss-Pdb Viewer: an environment for comparative protein modeling. *Electrophoresis* **1997**, *18* (15), 2714−2723.
(35) Bunker, B. C.; Rieke, P. C.; Tarasevich, B. J.; Campbell, A. A.; Fryxell, G. E.; Graff, G. L.; Song, L.; Liu, J.; Virden, J. W.; McVay, G. L. Ceramic thin-film formation on functionalized interfaces through biomimetic processing. *Science* **1994**, *264* (5155), 48−55.
(36) Kato, H.; Nakamura, A.; Takahashi, K.; Kinugasa, S. Accurate size and size-distribution determination of polystyrene latex nanoparticles in aqueous medium using dynamic light scattering and asymmetrical flow field flow fractionation with multi-angle light scattering. *Nanomaterials* **2012**, *2* (1), 15−30.
(37) Makarov, V. V.; Makarova, S. S.; Love, A. J.; Sinitsyna, O. V.; Dudnik, A. O.; Yaminsky, I. V.; Taliansky, M. E.; Kalinina, N. O. Biosynthesis of stable iron oxide nanoparticles in aqueous extracts of Hordeum vulgare and Rumex acetosa plants. *Langmuir* **2014**, *30*, 5982−5988.
(38) Olivares, O.; Likhanova, N. V.; Gomez, B.; Navarrete, J.; Llanos-Serrano, M. E.; Arce, E.; Hallen, J. M. Electrochemical and XPS studies of decylamides of alpha-amino acids adsorption on carbon steel in acidic environment. *Appl. Surf. Sci.* **2006**, *252*, 2894−2909.
(39) Silva, A. B.; Agostinho, S. M. L.; Barcia, O. E.; Cordeiro, G. G. O.; D'Elia, E. The effect of cysteine on the corrosion of 304L stainless steel in sulphuric acid. *Corros. Sci.* **2006**, *48*, 3668−3674.
(40) Bereket, G.; Yurt, A. The inhibition effect of amino acids and hydroxy carboxylic acids on pitting corrosion of aluminum alloy **7075**. *Corros. Sci.* **2001**, *43*, 1179−1195.
(41) Wang, K.; Zhang, J.; Lou, L.; Yang, S.; Chen, Y. UV or visible light induced photodegradation of AO7 on TiO2 particles: the influence of inorganic anions. *J. Photochem. Photobiol., A* **2004**, *165* (1−3), 201−207.
(42) Lassoued, A.; Dkhil, B.; Gadri, A.; Ammar, S. Control of the shape and size of iron oxide (α-Fe2O3) nanoparticles synthesized through the chemical precipitation method. *Results Phys.* **2017**, *7*, 3007−3015.
(43) Pauling, L.; Hendricks, S. B. The crystal structures of hematite and corundum. *J. Am. Chem. Soc.* **1925**, *47* (3), 781−790.
(44) Syvinski, W.; McCarthy, G. *ICCD Grant-in-Aid*; North Dakota State University: Fargo, ND, USA, 1990.
(45) Zboril, R. Mechanism of Fe2O3 Formation during Thermal Decomposition of FeSO4, 7H2O. Doctoral Dissertation, Ph. D. Thesis, Olomouc.
(46) Patterson, A. L. The Scherrer formula for X-ray particle size determination. *Phys. Rev.* **1939**, *56* (10), 978−982.
(47) Yu, J.; Yu, X.; Huang, B.; Zhang, X.; Dai, Y. Hydrothermal synthesis and visible-light photocatalytic activity of novel cage-like ferric oxide hollow spheres. *Cryst. Growth Des.* **2009**, *9* (3), 1474−1480.
(48) Wang, X. I.; Wu, J.; Li, P.; Wang, L.; Zhou, J.; Zhang, G.; Li, X.; Hu, B.; Xing, X. Microenvironment-responsive magnetic nanocomposites based on silver nanoparticles/gentamicin for enhanced biofilm disruption by magnetic field. *ACS Appl. Mater. Interfaces* **2018**, *10*, 34905−34915.
(49) Kragh-Hansen, U. Molecular aspects of ligand binding to serum albumin. *Pharmacol. Rev.* **1981**, *33* (1), 17−53.
(50) Sekar, G.; Haldar, M.; Thirumal Kumar, D.; George Priya Doss, C.; Mukherjee, A.; Chandrasekaran, N. Exploring the interaction between iron oxide nanoparticles (IONPs) and human serum albumin (HSA): spectroscopic and docking studies. *J. Mol. Liq.* **2017**, *241*, 793−800.
(51) Dong, C.; Ma, S.; Liu, Y. Studies of the interaction between demeclocycline and human serum albumin by multi-spectroscopic and molecular docking methods. *Spectrochim. Acta, Part A* **2013**, *103*, 179−186.

https://doi.org/10.1021/acsomega.3c05743
ACS Omega 2023, 8, 48775−48786